Enhancing Ground-Penetrating Radar (GPR) Data Resolution Through Weakly Supervised Learning

Dawei Liu⬝, Mei Zhou, Xiaokai Wang⬝, *Member, IEEE*, Zhensheng Shi, Mauricio D. Sacchi⬝, *Member, IEEE*, Wenchao Chen⬝, Zhaodan Liu, and Xian Wang

Abstract—Ground-penetrating radar (GPR) is a pivotal non-invasive tool that yields subsurface images critical to archeology, near-surface characterization, geotechnical studies, and disaster response. The antenna central frequency of the GPR system has a significant impact on penetration depth and resolution. Lower antenna frequencies penetrate deeper but at lower resolutions, while higher frequencies offer detailed images at reduced depths. Therefore, improving the resolution of low-frequency radar with increased detection depth is an essential research focus. Inspired by image super-resolution advancements, supervised deep learning methods that rely on strictly paired training data have achieved remarkable success. However, acquiring such paired samples in practical scenarios is often a formidable challenge. To tackle this, we propose a novel resolution enhancement technique through weakly supervised learning, effectively addressing the scarcity of strictly paired samples in real-world situations. We utilize two sets of antennas with different central frequencies to construct our training data, with a low-frequency antenna as input and a high-frequency antenna as the learning target. A cycle-consistent generative adversarial network (Cycle-GAN) is trained to discern the mapping between low-resolution inputs and unpaired high-resolution data. The refined network is then employed to improve low-frequency GPR data resolution. Our work is validated on synthetic and real-world datasets. The proposed method effectively strengthens critical high-frequency details for finer imaging and broadens the frequency bandwidth. Significantly, it enhances resolution without compromising the detection depth of low-resolution GPR data, marking a substantial advancement in subsurface imaging technology.

Index Terms—Cycle-consistent adversarial network, ground-penetrating radar (GPR), resolution, signal processing, weakly supervised learning.

I. INTRODUCTION

GROUND-PENETRATING radar (GPR) utilizes electromagnetic waves to explore subsurface structures. As a noninvasive imaging technique, GPR provides high-resolution subsurface profiles, proving invaluable in sedimentology [1], [2], archeology [3], [4], military reconnaissance [5], and disaster management [6]. High temporal resolution in GPR recordings is essential for precise stratigraphic interpretation of reflection images. It facilitates the detailed identification and characterization of subsurface structures, thereby improving subsurface evaluation reliability.

The performance of GPR, specifically its penetration depth and resolution, is affected by various factors. Key among these are the characteristics of the transmitter pulse [7], [8], and the design of the transmitter–receiver system [9]. Additionally, the electromagnetic properties of various media can induce ground filtering effects, leading to different levels of wave attenuation and a consequent decrease in resolution with increased depth. These factors collectively cause amplitude distortions and time delays, distorting the actual subsurface reflectivity profile. In practical exploration, a fundamental compromise emerges between resolution and penetration depth. High-frequency GPR antennas yield finer resolution but suffer from rapid energy attenuation, limiting exploration depth. Conversely, low-frequency GPR antennas, while offering enhanced penetration, deliver data with comparatively lower resolution. Consequently, any GPR system based on a singular central frequency must reconcile this inherent trade-off between the desired resolution and the depth of investigation.

Various signal processing methods have been proposed to enhance the GPR imaging capabilities constrained by a single central frequency, particularly in complex subsurface geometries. Traditional approaches include deconvolution, inverse Q filtering, spectral whitening, and the time-frequency transform method. Deconvolution [10], [11], [12], [13] is the inverse operation of the classic convolutional model, seeking to extract the original spike series from a convolved trace given the wavelet. However, geological complexities that deviate from idealized convolutional assumptions often undermine its effectiveness, yielding suboptimal results. Inverse Q filtering attempts to compensate for velocity dispersion and high-frequency energy dissipation during wave traveling, but it relies heavily on precise Q estimations, which are notoriously tricky to obtain [14], [15]. Spectral whitening, a more straightforward approach, avoids complex Q estimations but fails to rectify phase distortions [16], [17], [18]. In addition, as a frequency-dependent method, it inadvertently boosts noise levels since the amplified high-frequency components it targets are often occupied by noise, diminishing the overall fidelity of the GPR image. A common workaround involves applying a

time-varying bandpass filter to mitigate these issues. Advanced time-frequency transform techniques, such as the S transform [19], short-time Fourier transform [20], and wavelet transform [21], [22], are employed to enhance GPR resolution. While they are effective, the challenge of selecting appropriate model parameters persists [23], [24]. The burgeoning field of deep learning offers a promising alternative by acquiring prior knowledge from end-to-end learning to sidestep the parameter selection issue [25], [26], [27], [28], [29], [30], [31], [32], [33]. Notable implementations on GPR resolution enhancement include U-net [34], residual-in-residual structure [35], and InvNet [36]. While these supervised deep learning methods hold promise for advancing GPR resolution, their efficacy is contingent upon the availability of extensive, high-quality training datasets, which are often scarce due to the complex nature of subsurface environments.

Recent advancements in GPR technology have seen the emergence of multichannel (or multiarray) systems capable of providing multifrequency datasets. These modern systems, such as the sweep-frequency radar for the Mars2020 mission [37] and the dual-frequency radar for the Chang'E4 mission [38], offer a promising approach to address the inherent trade-off between penetration depth and resolution encountered with single central frequency systems. Data fusion methodologies have become indispensable to fully leverage the rich information garnered from antennas operating at different central frequencies. Traditional methods, including statistical techniques [39], wavelet transforms [40], genetic algorithms [41], and tomographic inversions [42], have been successfully employed to enhance GPR datasets. However, these approaches often require extensive preprocessing and struggle to transition smoothly between the merged sections from different frequency profiles. Recent innovations in deep learning, particularly those involving recurrent neural networks [43], [44], have been proposed to address the data merging issue more seamlessly. However, they hinge on the availability of precisely matched datasets in one-to-one correspondence. This necessitates an exacting alignment of survey paths, typically along a straight line, which is not only labor-intensive but also challenging on steep or rough terrains. Furthermore, antennas of different frequencies typically have distinct sampling parameters due to instrumentation variability and operational constraints. These necessitate a meticulous data calibration process to ensure the fidelity of multifrequency data fusion, which also could introduce data differences. Additionally, collecting paired samples may not be feasible in certain situations, such as when dealing with historical data or studying rare or rapidly evolving phenomena. Therefore, there is an urgent need for weakly supervised deep learning methods to overcome these challenges, improving flexibility and scalability in various real-world applications. Weakly supervised learning involves training networks with unpaired data, where the learning target is available but not explicitly matched with the input data. It aims to infer the mapping from the input distribution to the learning target distribution. This method contrasts with semi-supervised learning, which combines a small amount of fully labeled data with a larger volume of unlabeled data but does not involve the challenge of label imprecision inherent in weakly supervised settings.

To mitigate the challenges in acquiring precisely matched low- and high-resolution GPR samples in practical engineering, we draw inspiration from image processing, where style transfer techniques between unpaired images have demonstrated potential for resolution enhancement [45]. Similarly, in seismic data processing, unpaired training strategies have shown promise [46]. Building on these insights, we propose a weakly supervised learning framework using a cycle-consistent generative adversarial network (Cycle-GAN). This innovative network learns the mapping relationship from low- to high-resolution GPR data domains without paired samples. Accordingly, it streamlines data collection and makes flexible data acquisition possible, eliminating the requirement for precise path alignment. Moreover, this unpaired training strategy focuses on learning distinctive features directly from the target data, thus sidestepping the intensive preprocessing required by traditional methods, such as amplitude equalization and balance. Like other learning-based methods, its performance continues to evolve as more high-resolution data becomes available. Standing on [46], we significantly improve the stability of resolution enhancement by incorporating an additional cycle structure. After fine-tuning, the trained network effectively enhances the resolution of the entire low-frequency GPR image in a single pass, avoiding unwanted "cut and paste" artifacts typically introduced by combined windows of traditional methods. Furthermore, the network inference process is highly efficient, which is advantageous for handling large datasets from multifrequency antennas. Validated on simulated and real-world datasets, our technique consistently enhances high-frequency detail and extends bandwidth without causing phase distortions. Most notably, it significantly improves resolution while preserving the detection depth of low-resolution GPR data, underscoring its utility for advanced GPR applications.

The remainder of the article is organized as follows. Section II outlines the methodology employed throughout the study. Section III presents the results of resolution enhancement experiments conducted on both simulated and field seismic data, demonstrating the superior performance of the proposed method. Then, we discuss the limitations of the current approach and suggest potential avenues for future research in Section IV. Finally, the conclusion is presented in Section V.

II. METHOD

Building upon the CycleGAN framework's capacity for image translation without paired training data, this section outlines the overall workflow for weakly supervised learning and refines its architecture and loss function to improve GPR data resolution using unpaired high-frequency samples.

A. GPR Resolution Enhancement Workflow Using Weakly Supervised CycleGAN

This section delineates the workflow for enhancing GPR data resolution through a weakly supervised CycleGAN.
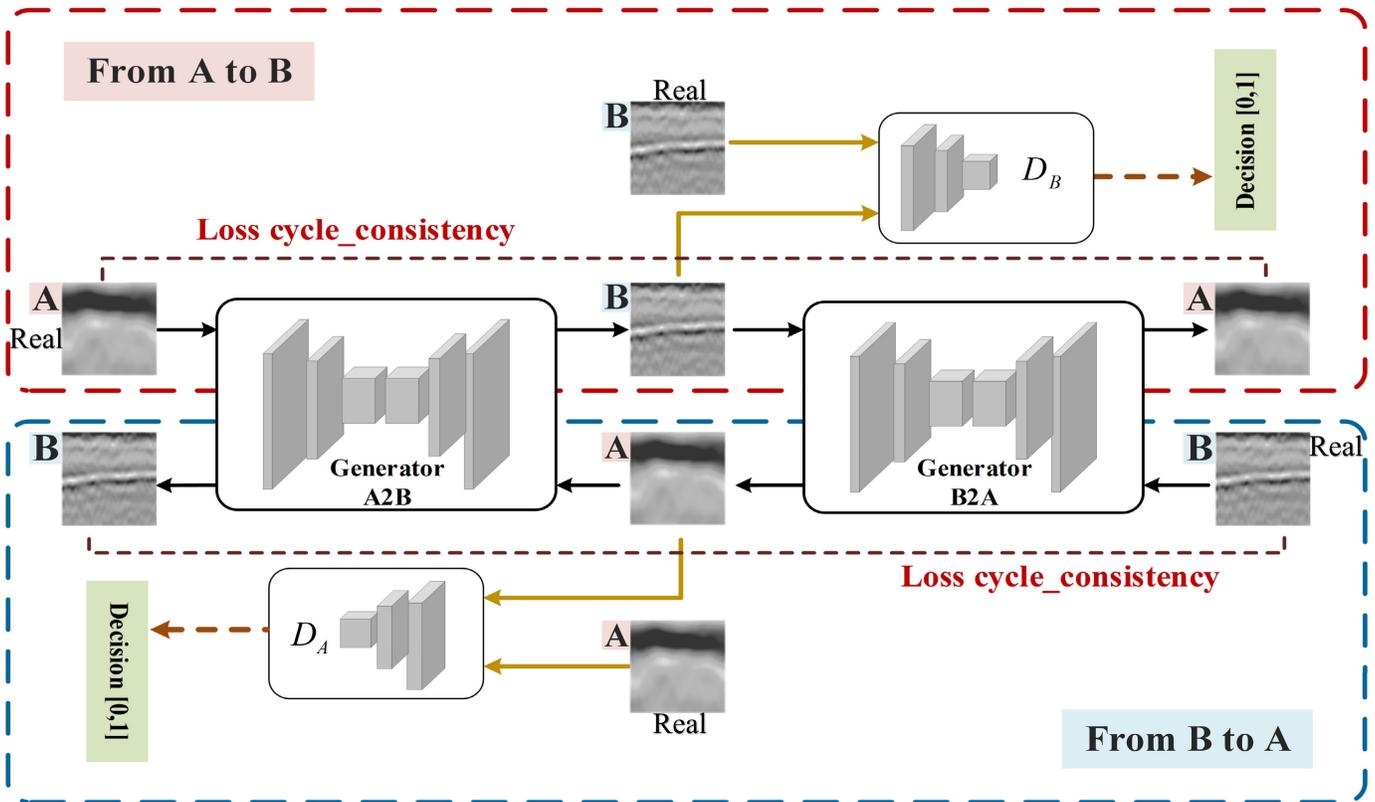
Fig. 1. Workflow of the CycleGAN network for enhancing GPR data resolution. "A" represents low-resolution data, and "B" signifies high-resolution data. The term "Real" refers to patches cropped from real-world field data, distinguishing them from data generated by the generator.

Our method utilizes low-resolution GPR inputs to synthesize data comparable to high-resolution GPR samples without requiring precise matching between training inputs and target outputs. The strength of this approach lies in the CycleGAN's ability to transform data from a low-resolution GPR data domain (referred to as $\mathcal{A}$) to a high-resolution domain (referred to as $\mathcal{B}$), leveraging the model's inherent feature adaptation capabilities.

Fig. 1 depicts the tailored workflow of CycleGAN employed in this research. The architecture comprises two GANs arranged in a symmetric configuration, each containing a generator and a discriminator. The generator G_{A2B} is tasked with learning the transformation from the low-resolution data distribution to the high-resolution domain, thereby translating samples from domain $\mathcal{A}$ to domain $\mathcal{B}$. Conversely, the generator G_{B2A} performs the inverse mapping, converting high-resolution GPR data back to the low-resolution domain $\mathcal{A}$. The discriminator D_B guides the generator G_{A2B} by differentiating between actual high-resolution data and synthesized outputs, promoting the adversarial learning process that drives the synthesis of more authentic high-resolution GPR images. Simultaneously, the discriminator D_A assesses the authenticity of G_{B2A}'s output, generating credible low-resolution GPR images. This dual arrangement facilitates a robust adversarial feedback loop, where each generator not only strives to produce realistic images but also learns to reconstruct the original input from its own outputs, ensuring fidelity and consistency. This symmetric reconstruction process fosters a robust feature learning environment.

It inherently encourages the preservation of essential features, which is critical for generating realistic high-resolution GPR data that retain the integrity of the subsurface information.

We further elucidate the workflow with an example of one unidirectional data flow from domain $\mathcal{A}$ to domain $\mathcal{B}$.

1) *Initial input:* Low-resolution GPR samples from domain $\mathcal{A}$ are introduced to the generator G_{A2B}.
2) *High-resolution generation:* The generator G_{A2B} processes the inputs to synthesize high-resolution outputs, aiming to emulate the characteristics of high-resolution GPR data in domain $\mathcal{B}$.
3) *Reconstruction:* The synthesized high-resolution data is subsequently fed into the generator G_{B2A}, which attempts to reconstruct the original low-resolution data. This step is crucial as it enforces the preservation of key features during the resolution enhancement process.
4) *Discrimination and iteration:* Discriminators D_A and D_B assess the synthesized data and reconstructed data, respectively. Their role is to guide the adversarial training by providing critical feedback on the realism of the generated data. This feedback prompts iterative refinement of the network parameters, leading to enhanced fidelity and authenticity in the GPR images produced by the network.

The adversarial training process is a carefully orchestrated sequence where the discriminators are initially trained to distinguish between actual and synthesized data, followed by the training of the generators based on the feedback from the discriminators. This iterative process continues until the
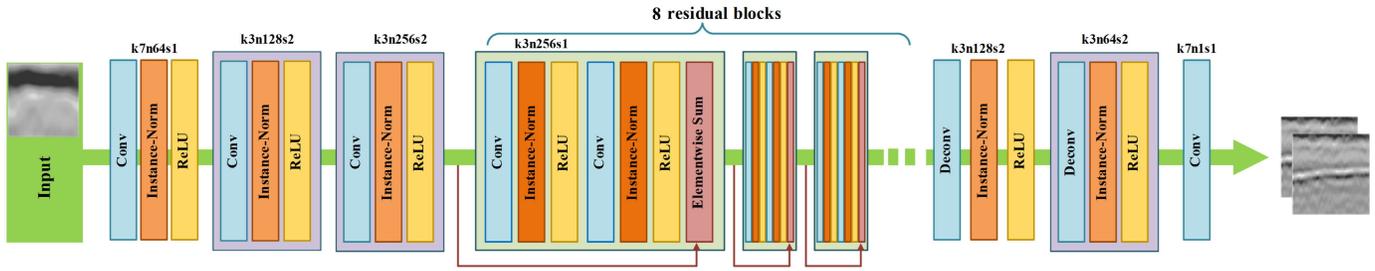
Fig. 2. Architecture of generator G_{A2B}. The numbers following the symbols k, n, and s indicate the specific parameters of the convolutional layer. Specifically, "k7n64s1" refers to a convolution layer with 64 filters, where the spatial size is 7 and the stride is 1.
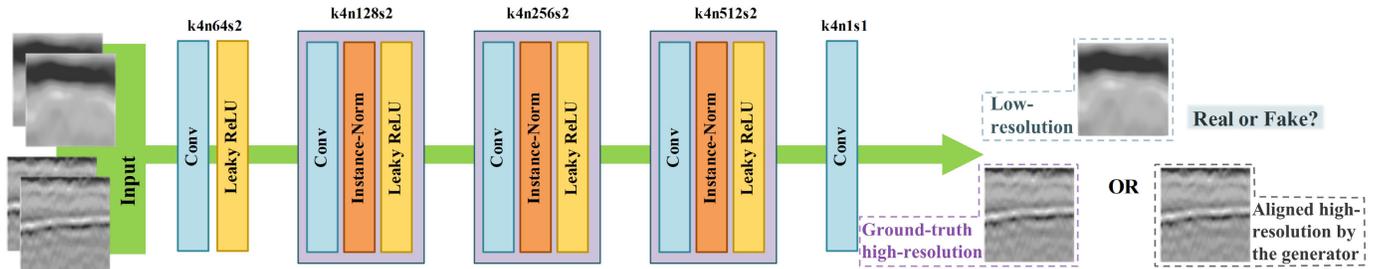

Fig. 3. Architecture of discriminator D_B. This component is crucial for guiding the updates of generator G_{A2B} by differentiating between actual high-resolution data and generated outputs, ensuring the progressive refinement of generated images toward authentic high-resolution quality.

network achieves a Nash equilibrium state, indicating that both the generators and discriminators are optimized to their full potential.

B. Network Architecture

We refine the CycleGAN architecture proposed by Zhu et al. [47] to address the challenge of enhancing the resolution of GPR data. Our improvements are detailed in the generator and discriminator components, ensuring a comprehensive upgrade to the workflow's capabilities.

Image super-resolution is one of the pioneering applications of deep learning, paving the way for the revolutionary integration of CycleGAN in enhancing image quality. Within this context, the role of generators is critical, as they synthesize the fine details that significantly impact the performance of resolution improvement tasks. Our generator network is thoughtfully engineered to mirror the successful architectures in single-image super-resolution, as explored by Zhang et al. [48]. Detailed in Fig. 2, it incorporates convolutional layers, instance normalization layers, activation functions, and residual blocks, each meticulously integrated to facilitate the generation of high-resolution GPR images.

The generator begins refining input GPR data through a cascade of convolutional layers, each followed by instance normalization and rectified linear unit (ReLU) activation functions. This sequence efficiently extracts sophisticated features, condensing the raw data into essential feature spaces that encapsulate the crucial subsurface information while compressing the data dimensions. To counteract the potential information loss inherent in deep networks, we strategically position eight residual blocks within the generator. These blocks are designed to preserve the intricate details

of GPR data, safeguarding subsurface structural fidelity. They also mitigate the vanishing gradient issue commonly encountered with increasing network depth, ensuring consistent gradient propagation throughout the training process. The generator culminates with two deconvolutional layers that upscale the condensed feature representations back into a high-resolution format. This crucial step transforms the feature space into detailed GPR images that align with the target high-resolution domain. In addition, normalization plays a pivotal role throughout the network training. After careful consideration, we opt for instance normalization [49] over batch normalization [50] due to its superior performance in normalizing individual data samples. This normalization method is particularly advantageous for our application, as it helps to avoid the training instabilities and visual artifacts that batch normalization may introduce in deep networks. Moreover, it contributes to a faster and more stable network convergence, which is critical for efficiently training our model to produce high-fidelity GPR images.

In the discriminative phase of our CycleGAN framework, we utilize two PatchGAN [51] discriminators with identical structures. The PatchGAN discriminators are specifically proficient at detecting high-frequency components by concentrating on localized patches, thereby streamlining the model's complexity through a reduced parameter count without compromising its feature recognition capabilities. As illustrated in Fig. 3, our design incorporates multiple convolutional layers dedicated to feature extraction, culminating in a final convolutional layer outputting a grid of values. Each value corresponds to a discrete input patch, providing the assessment of the discriminator on the authenticity of each patch. The average of these values is then computed to determine the overall discrimination score. Following the earlier normalization approach,

instance normalization is applied to feature maps extracted from convolution layers. This choice is in harmony with the localized operational focus of PatchGAN, facilitating the discrimination process.

In summary, the architecture of our CycleGAN is tailored to enhance GPR data resolution by leveraging a generator that preserves essential details and an efficient discriminator that focuses on local features. The normalization technique ensures stable and fast convergence. This innovative architecture, combined with carefully formulated loss functions, directs the adversarial training to produce high-quality, high-resolution subsurface images.

C. Loss Functions

Under the guidance of the previously outlined workflow and network architecture, we now focus on the specifics of loss functions. These functions are pivotal in training, greatly shaping the overall training outcome. With unpaired training patches $a \in \mathcal{A}$ and $b \in \mathcal{B}$, the total CycleGAN loss function $\mathcal{L}_{\text{total}}$ is decomposed into three fundamental components: generative adversarial loss $\mathcal{L}_{\text{GAN}}$, cycle consistency loss $\mathcal{L}_{\text{cyc}}$, and multiscale structural similarity (MS-SSIM) loss $\mathcal{L}_{\text{MS-SSIM}}$. Each component fulfills a specific role in guiding the network toward generating high-fidelity GPR images.

The GAN loss is applied to both generators and discriminators to ensure that the generated data aligns with the target sample distribution. For improved training stability, we utilize the least squares loss, as suggested by Mao et al. [52], over the traditional negative log-likelihood approach [53]. The GAN loss for G_{A2B} and D_B, which encourages the generator to produce high-resolution GPR data that appears authentic to the discriminator, is defined as follows:

$$\mathcal{L}_{\text{GAN}}^{A2B}(G_{A2B}, D_B) = \mathbb{E}_{b \sim \mathbb{P}_{\mathcal{B}}}\left[D_B(b)^2\right] \\ + \mathbb{E}_{a \sim \mathbb{P}_{\mathcal{A}}}\left[(1 - D_B(G_{A2B}(a)))^2\right] \quad (1)$$

where $\mathbb{P}_{\mathcal{A}}$ and $\mathbb{P}_{\mathcal{B}}$ represent the distributions of the low-resolution and high-resolution GPR data domains, respectively. The function $G_{A2B}(a)$ denotes the generative process for the mapping $G_{A2B} : \mathcal{A} \rightarrow \mathcal{B}$, while $D_B(\cdot)$ is the discriminator's evaluation of the generated and target data. Similarly, the loss function for the inverse transformation from $\mathcal{B}$ to $\mathcal{A}$ is

$$\mathcal{L}_{\text{GAN}}^{B2A}(G_{B2A}, D_A) = \mathbb{E}_{a \sim \mathbb{P}_{\mathcal{A}}}\left[D_A(a)^2\right] \\ + \mathbb{E}_{b \sim \mathbb{P}_{\mathcal{B}}}\left[(1 - D_A(G_{B2A}(b)))^2\right]. \quad (2)$$

These two loss functions are integral to $\mathcal{L}_{\text{GAN}}$, compelling the generators to create data that is indistinguishable from the actual target samples, thereby achieving a more stable and reliable GPR data enhancement.

To avoid generating unrealistic and meaningless samples and maintain the integrity of the generated data concerning the original sample distribution, we employ the cycle consistency loss function. The cycle consistency loss measures the difference between the original data and the reconstruction from transformed data. It ensures that the transformations between the two domains are reversible, maintaining a consistent mapping. Given the dual-generator architecture of our model,
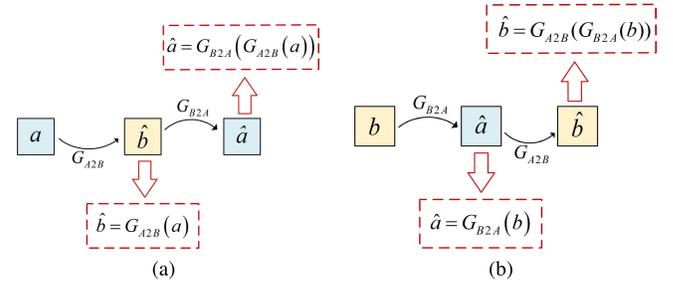

Fig. 4. Diagram of cycle consistency loss. (a) Data flow starting from $\mathcal{A}$ to $\mathcal{B}$. (b) Data flow starting from $\mathcal{B}$ to $\mathcal{A}$.

this loss is split into two components: from $\mathcal{A}$ to $\mathcal{B}$ and from $\mathcal{B}$ to $\mathcal{A}$, as conceptualized in Fig. 4. The former is illustrated in Fig. 4(a), which traces the journey of low-resolution GPR data as it is first elevated to a high-resolution state by G_{A2B} and subsequently reverted to its original domain via G_{B2A}. Essentially, this is characterized by the transformation $a \rightarrow G_{A2B}(a) \rightarrow G_{B2A}(G_{A2B}(a)) \approx a$. Conversely, Fig. 4(b) depicts the transformation of high-resolution data back to its initial form, which can be represented as $b \rightarrow G_{B2A}(b) \rightarrow G_{A2B}(G_{B2A}(b)) \approx b$. The interplay of these two cycle consistency losses imposes a robust constraint on the generators, ensuring that the model preserves the core attributes of the GPR data through the transformation processes. Based on the $\mathcal{L}_1$ norm, the discrepancy between the original and reconstructed GPR data can be evaluated as follows:

$$\mathcal{L}_{\text{cyc}}(G_{A2B}, G_{B2A}) = \mathbb{E}_{a \sim \mathbb{P}_{\mathcal{A}}}[\|G_{B2A}(G_{A2B}(a)) - a\|_1] \\ + \mathbb{E}_{b \sim \mathbb{P}_{\mathcal{B}}}[\|G_{A2B}(G_{B2A}(b)) - b\|_1]. \quad (3)$$

To address the limitations of cycle consistency loss in preserving structural integrity during data transformations, we incorporate an additional structural consistency loss function. The MS-SSIM [54] is employed herein, assessing the internal structure, contrast, and luminance between the original and generated data. It ensures that the transformation process maintains the data structural fidelity by maximizing the similarity across the transformation cycle. The structural consistency loss is mathematically formulated as follows:

$$\mathcal{L}_{\text{MS-SSIM}}(G_{A2B}, G_{B2A}) \\ = \mathbb{E}_{a \sim \mathbb{P}_{\mathcal{A}}}[1 - \text{MS-SSIM}(G_{B2A}(G_{A2B}(a)), a)] \\ + \mathbb{E}_{b \sim \mathbb{P}_{\mathcal{B}}}[1 - \text{MS-SSIM}(G_{A2B}(G_{B2A}(b)), b)]. \quad (4)$$

Integrating the cycle consistency and structural consistency losses imposes robust constraints that guide the generators toward producing high-fidelity transformations. The total objective function is composed of the aforementioned loss components

$$\mathcal{L}(G_{A2B}, G_{B2A}, D_A, D_B) = \mathcal{L}_{\text{GAN}}^{A2B}(G_{A2B}, D_B) \\ + \mathcal{L}_{\text{GAN}}^{B2A}(G_{B2A}, D_A) \\ + \lambda_1 \mathcal{L}_{\text{cyc}}(G_{A2B}, G_{B2A}) \\ + \lambda_2 \mathcal{L}_{\text{MS-SSIM}}(G_{A2B}, G_{B2A}) \quad (5)$$

where the trade-off weights λ_1 and λ_2 are carefully calibrated through heuristic experimentation to delicately balance the model's focus and achieve the best performance. We minimize this objective function by employing the Adam gradient
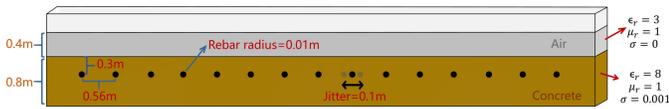
Fig. 5. Simulation model example with rebars placed in deep positions. Rebar placements are perturbed horizontally to generate unpaired low- and high-resolution datasets, respectively.

descent method [55], converging this model to a solution that captures the subtle variances and critical features for effective GPR image enhancement.

III. EXAMPLES

A. Simulated Data Example: Unpaired GPRMax Data

We first verify the efficacy of our proposed GPR resolution enhancement technique using simulated data. Traditional convolutional models often fail to accurately model GPR wave propagation in complex subsurface environments. Hence, this study leverages the GPRMax platform [56], which employs realistic electromagnetic wave propagation techniques to generate simulations that closely resemble real-world subsurface conditions. Using GPRMax-simulated data increases the credibility of our experimental findings and substantiates the validity of our method.

We develop two distinct GPR simulation models that incorporate concrete layers and subsurface rebars at varying depths. We first evaluate our proposed method using the more straightforward first model, establishing a baseline for performance. Subsequently, we employ a second, more intricate model to challenge the network under complex conditions, showcasing the high adaptability and robustness of our technique. Both models share the same parameters, except for the varying depths of an air layer and rebars. In these models, the rebars have a radius of 0.01 m. The concrete is defined by a relative permittivity of $\epsilon_r = 8$, a conductivity of $\sigma = 0.001$, and a permeability of $\mu_r = 1$.

Fig. 5 illustrates the first GPRmax model, where rebars are deeply embedded and horizontally aligned. The first model features an air layer of 0.4 m atop a 0.8-m concrete layer, with rebars positioned 0.3 m beneath the concrete surface. The rebar spacings for constructing low- and high-resolution datasets vary to accommodate unpaired training. Each model introduces a perturbation ranging from −0.1 to 0.1 m to the standard 0.56 m interval. This also increases training data diversity and helps the model adapt to input disturbances, improving its stability and mitigating overfitting.

Based on two perturbated versions of Fig. 5, we use two Ricker wavelets [57] of different frequencies as wave propagation sources to simulate low-resolution and high-resolution GPR datasets, respectively. For low-resolution data, we employ a 500-MHz center frequency antenna. In parallel, a 900-MHz antenna simulates high-resolution data under the same conditions but with a different model perturbation, exploiting the superior resolution capabilities of higher frequencies. The receivers, placed on the ground, capture the reflected waves as the electromagnetic signal propagates. As a result, we obtain two unpaired datasets.

We trim the low-frequency GPR data to create a training dataset, with the high-frequency GPR data acting as the
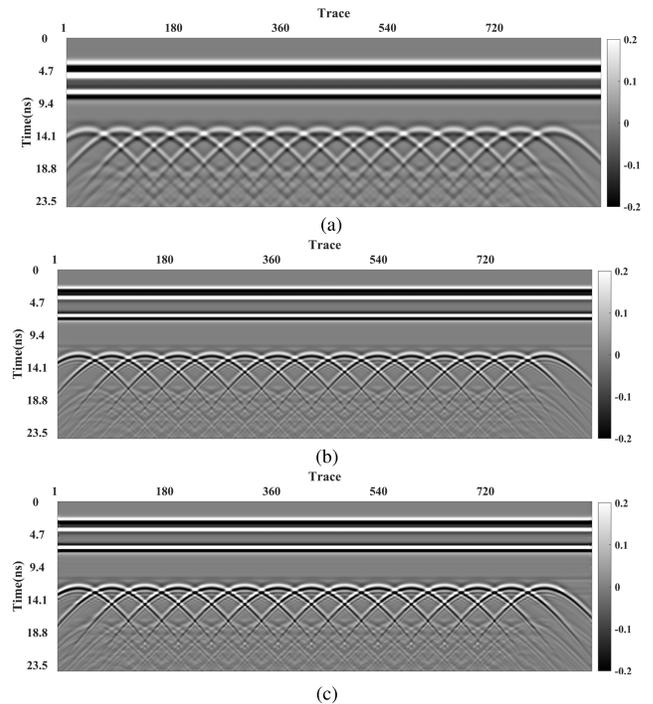

Fig. 6. GPR data based on the deep-rebar model. (a) Simulated low-resolution data. (b) Simulated high-resolution data. (c) Generated high-resolution data using weakly supervised learning.

learning target, thus enabling an evaluation of our proposed CycleGAN's efficacy on simulated data. Then, we randomly shuffle the sample patches and their non-paired learning targets before inputting them into the network for training. The network training parameters are set as follows: $\lambda_1 = 1e^{-3}$, $\lambda_2 = 2e^{-4}$, a patch size at 256×256, a dataset size of 500 patches, a batch size of 4, a learning rate of $2e^{-4}$, and a training duration of 150 epochs. After training, we introduce additional modest variations in the rebar intervals based on Fig. 5, differing from the models for generating training data, and create low-resolution data to validate the transformation from low-resolution to high-resolution GPR data.

The trained network is applied to the low-resolution in Fig. 6(a), which is also produced by a 500-MHz center frequency antenna. The rebars, positioned further from the concrete surface, generate hyperbolic reflections clearly distinguishable from the strong direct waves along the time axis. We also generate high-resolution data on the same model with the 900-MHz antenna for comparison. As illustrated in Fig. 6(b), these reflections, considered valid signals, manifest in a distinct structural pattern. A side-by-side comparison reveals that the low-frequency antenna produces data with diminished resolution, leading to blurry reflections. As demonstrated in Fig. 6(c), our method significantly enhances the resolution of the GPR data. Notably, the processed data showcases sharper and clearer waveforms than the original low-resolution GPR data's coarser reflected waves. Echoing the clarity of the simulated high-resolution radar data, the refined waveforms are more pronounced, signifying a successful enhancement in resolution.

The second model poses a more significant challenge in discerning useful information and enhancing resolution.
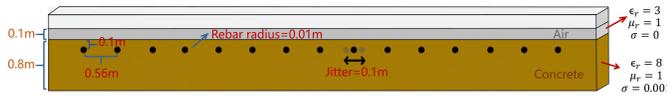
Fig. 7. Simulation model example with rebars placed in shallow positions. Rebar placements are perturbed horizontally to generate unpaired low- and high-resolution datasets, respectively.
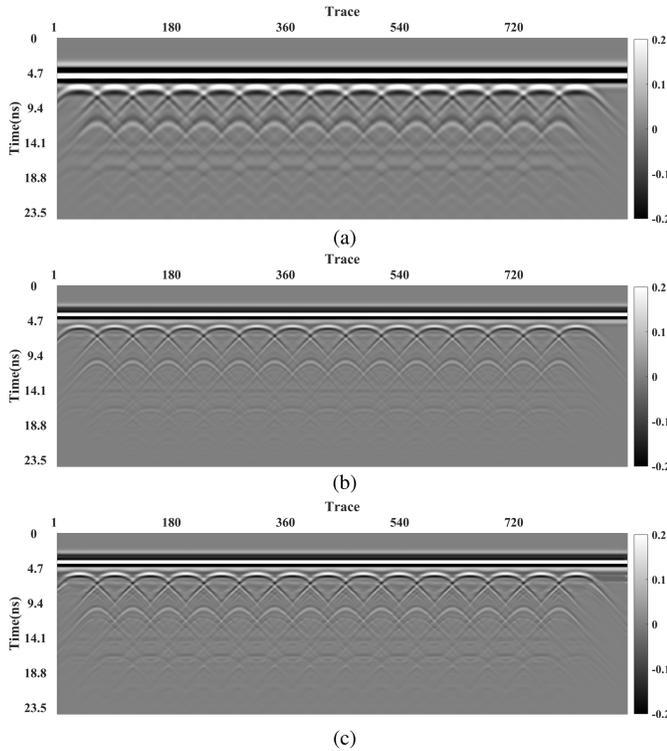

(a)

(b)

(c)

Fig. 8. GPR data based on the shallow-rebar model. (a) Simulated low-resolution data. (b) Simulated high-resolution data. (c) Generated high-resolution data using weakly supervised learning.
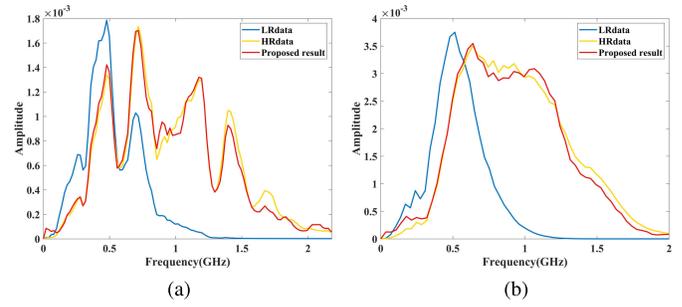

Fig. 9. Comparison of multitrace average amplitude spectra. (a) Deep-rebar model. (b) Shallow-rebar model.

Fig. 10. Illustration of experimental tunnel model.

As shown in Fig. 7, the rebars are located just 0.1 m from the concrete surface, and the air layer height is reduced to 0.1 m. It sets the rebars at a shallower depth, intensifying electromagnetic interactions with the concrete layer and complexing the subsurface data profile. We first train the network consistently with established strategies and parameters. Then, a model based on Fig. 7 is introduced for network testing and produces compared results. This model also includes intentional jitters in rebar spacing to better mimic real-world scenarios. The simulated comparative GPR data with Ricker wavelets of different frequencies are more complicated than the previous model in Fig. 5, as shown in Fig. 8(a) and (b). Testing our network on Fig. 8(a) outcomes Fig. 8(c). It clearly indicates that our proposed method markedly enhances the resolution of low-resolution GPR simulations. Reflected waveforms from buried objects are more evident. Moreover, the obtained radar profiles align closely with high-resolution simulated data, signifying the effective resolution improvement achieved by our technique.

The amplitude spectrum analysis presented in Fig. 9 further confirms that our method not only enhances GPR resolution but also ensures fidelity to the subsurface characteristics, mirroring high-resolution synthesized benchmarks. These results underscore the robustness of our approach and its promising application in real-world field data interpretation, demonstrating a significant step forward in subsurface exploration technology.

B. Real-World Example 1: Engineered Tunnel Structure Detection

Tunnels are vital for underground transportation but are susceptible to deterioration over time, such as the development of cracks or voids behind their linings, which threaten structural integrity and safety. GPR has become a pivotal tool for evaluating the health of these structures [58]. To explore this application, we apply our resolution enhancement method to data collected from a meticulously constructed tunnel model, with subsequent detailed analysis of the results. The model and its internal details are illustrated in Fig. 10. The controlled environment of the engineered tunnel allows for precise knowledge of its internal structure, offering a solid foundation for method validation.

We use two GPR systems to acquire data from this model, obtaining low- and high-resolution datasets at 400 and 900 MHz, respectively. From these, we form a training dataset composed of 500 cropped, non-paired data pairs, each measuring 256×256 samples. To guarantee diversity within the sample set, we randomly shuffle the non-paired samples and their corresponding learning targets before inputting them into the network for training. The experimental setup parallels prior simulations, except for employing a batch size of 8 and a learning rate set to $1e^{-4}$.

Fig. 11 presents comparative graphs from the conducted survey. As illustrated in Fig. 11(a), the acquired low-resolution GPR data effectively images deep objects within the simulated tunnel environment but with compromised resolution. On the other hand, the high-resolution data shown in Fig. 11(b)
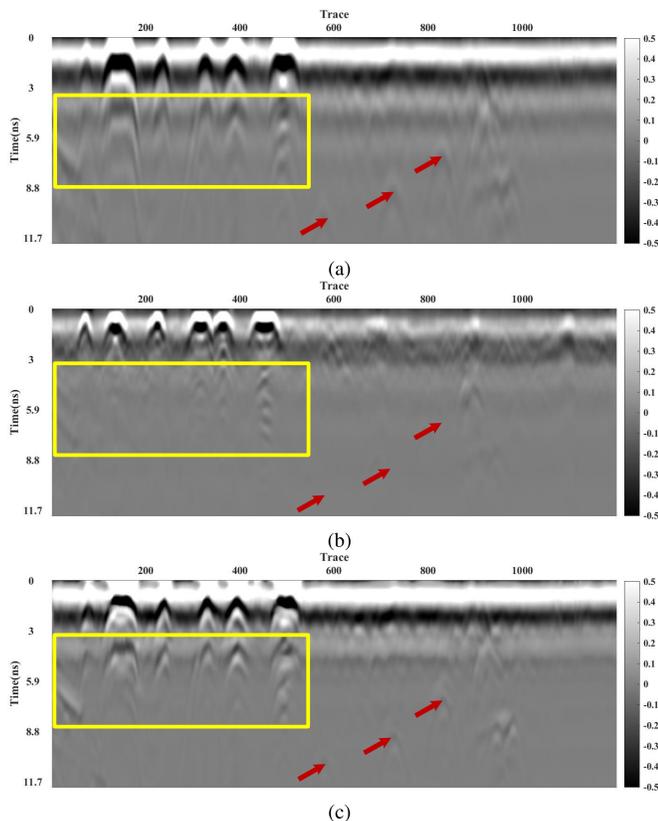
Fig. 11. GPR data based on the engineered tunnel model. (a) Acquired low-resolution data. (b) Acquired high-resolution data. (c) Generated high-resolution data using weakly supervised learning.
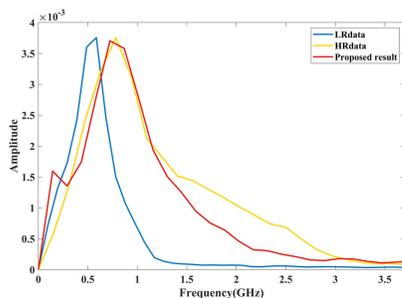

Fig. 12. Comparison of multitrace average amplitude spectrum.

captures finer details but at the expense of imaging depth, exemplifying a prevalent and challenging trade-off in practical field acquisition. The advancements achieved by our method, illustrated in Fig. 11(c), demonstrate a significant improvement in resolution at shallow depths, providing a clearer outline of the targets. The yellow boxes highlight areas where overlapping reflections previously obscured target signals due to the tailing phenomenon; these are now distinctly visible, significantly improving interpretability. Additionally, as the red arrows point out, the tunnel model contains three plastic pipes at different depths. The original high-resolution data barely reveals these objects, whereas our method clearly delineates them, showcasing a substantial resolution enhancement.

Fig. 12 presents the average amplitude spectrum comparison of the experimental data. Analysis of these spectra reveals

Fig. 13. Running track for collecting real-world datasets.

that the GPR data produced by our proposed method not only extends the frequency range but also closely mirrors the amplitude spectrum of the actual high-resolution measurements. This similarity suggests that our generated data attains a significant resolution enhancement. The simulated tunnel experiment validates our approach, showing that it achieves finer detail and accurate target detection in line with the known tunnel structure. This thorough assessment confirms the effectiveness and viability of our resolution enhancement technique.

C. Real-World Example 2: Running Track Assessment

The safety of public recreational areas, especially heavily trafficked playgrounds, has garnered widespread attention. Our study aims to contribute to this area by testing our method on a playground track.

1) Training Data Construction: The experimental data are collected from the East Track at Xi'an Jiaotong University, a standard eight-lane track with a lane width of 1.22 m, as shown in Fig. 13. We employ GPR systems at two distinct frequencies to explore the subsurface layers of different running lanes, yielding GPR data of diverse resolutions. To test the versatility of our method in complex data acquisition scenarios, different recording time parameters are employed. For low-resolution data, we utilize a 900-MHz GPR on the third plastic running lane. We set a recording time window of 24 ns, with 512 sampling points per trace and 100 traces/m. This process generates 8408 traces used to construct a 2-D profile, as depicted in Fig. 14(a). In contrast, the high-resolution data is acquired using a 2-GHz GPR on the fifth lane. This system employs a shorter recording time window of 12 ns (half that of the low-frequency GPR). It doubled the data density at 200 traces per meter, resulting in 16504 traces and a data size of $512 \times 16\,504$.

Though the exploration parameters differ between these datasets, our method requires only minimal calibration to adapt to this more realistic scenario. Our technique, grounded in weakly supervised learning, simplifies the process by eliminating the need for pairing training samples with labels. Essentially, it involves learning transformations between two different representations of the same target. The only requisite is that both low- and high-resolution GPR data align with the same subsurface structure depth. This alignment is pivotal
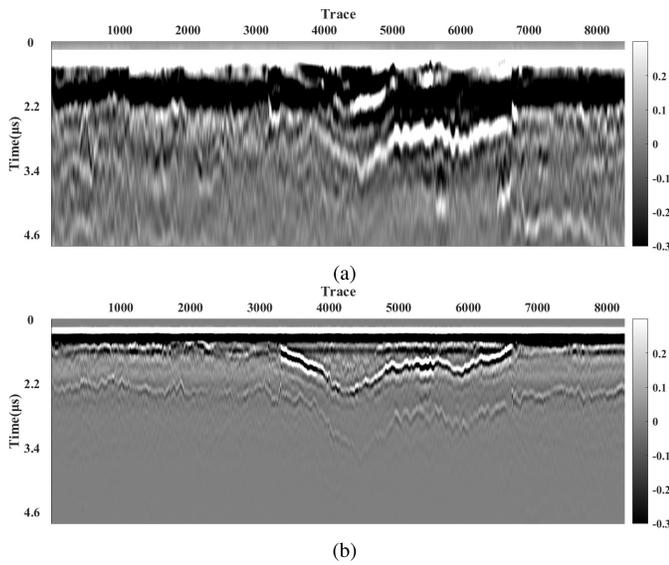
Fig. 14. Unpaired training data. (a) Low-resolution data acquired in the third running lane. (b) High-resolution data acquired in the fifth running lane.
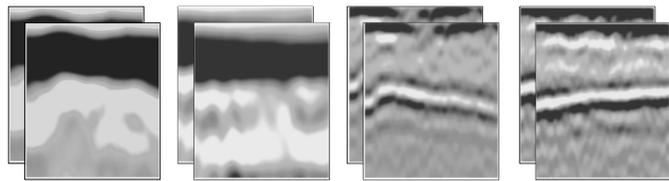

Fig. 15. Examples of cropped patches from the training dataset, with low-resolution data on the left and high-resolution data on the right.
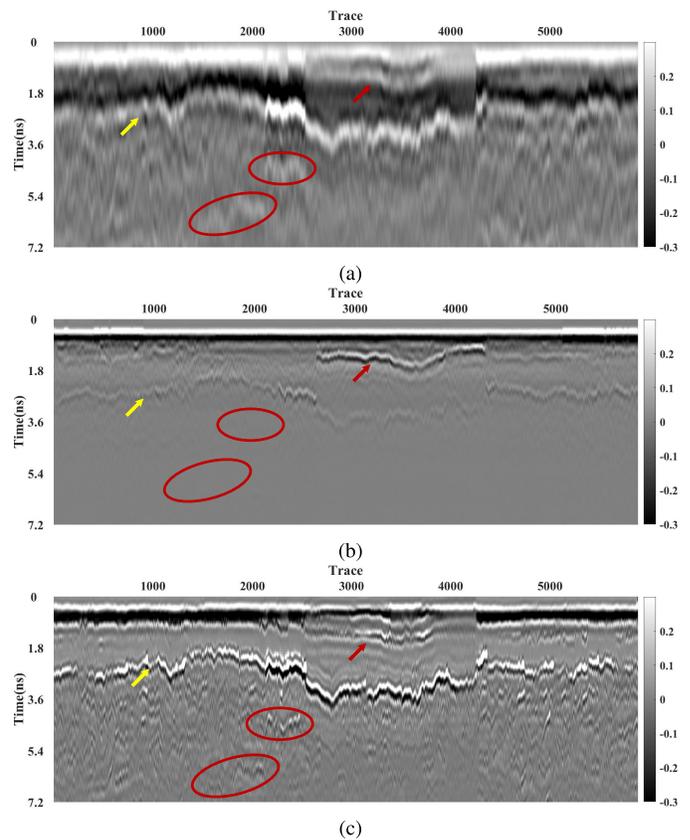

Fig. 16. Experimental results for second lane data. (a) Acquired low-resolution data. (b) Acquired high-resolution data. (c) Generated high-resolution data using weakly supervised learning.

as it safeguards depth information integrity for each dataset. To accomplish this, we apply linear interpolation to the low-resolution data, effectively aligning subsurface features with their unpaired high-resolution counterparts in the time domain. For spatial consistency, we employ equal interval sampling to downsample the high-resolution data and produce Fig. 14(b). This step guarantees that spatial information is preserved and consistent across the transformed representations, thereby enhancing the accuracy of our weakly supervised learning approach.

In addition, Fig. 14 exemplifies a prevalent and challenging trade-off in practical field acquisition: the acquired low-resolution GPR data effectively image deep objects but with compromised resolution; the high-resolution data capture finer details but at the expense of imaging depth. We focus on learning the mapping relationship between low-resolution and high-resolution data, enabling the network to enhance the resolution of deep subsurface images without sacrificing depth penetration. Considering the interference of strong direct waves in the GPR data, which can hinder deep information mapping, we apply nonlinear data gain to both low- and high-resolution GPR data. This step compensates for signal attenuation during propagation. The preprocessed GPR data are randomly cropped from the upper half and normalized for training. High-resolution GPR data patches function as training targets, while low-resolution data are used as input for CycleGAN. Fig. 15 showcases cropped patches from the constructed dataset. Upon completing network training,

we evaluate the efficacy and suitability of our method using actual low-resolution GPR data obtained from other running lanes. The experimental setup parallels prior simulations and the critical changed parameters for this experiment include a dataset size of 1000, a patch size of 128×128, a batch size of 8, a learning rate of $1e^{-4}$, and a total of 100 epochs.

2) Testing on Second Lane Data: Fig. 16 offers a comparative analysis of data from the second lane. Fig. 16(a) depicts the low-resolution GPR data with dimensions of 512×5916. These data are directly fed into the trained CycleGAN for testing. To provide a basis for comparison, we collect actual high-resolution GPR data, primarily offering enhanced resolution information for shallow subsurface positions, as depicted in Fig. 16(b). Our results are illustrated in Fig. 16(c). A comparison of these three GPR data profiles reveals the significant resolution enhancement our method brings about at shallow subsurface positions, specifically at the location marked 2.7 ns. The subsurface structures generated by our method closely mirror the high-resolution GPR data, effectively distinguishing subsurface information from 0 to 2.7 ns, as pointed out by the yellow arrow.

Additionally, our method clearly outlines the collapse zone, as indicated by the red arrow. In contrast to the actual high-resolution data, which falls short in providing information on deeper layers, our proposed method leverages the input low-resolution GPR data to unveil more intricate deep geological structures (highlighted within the red ellipses). The subsurface information aligns with the trend of the original
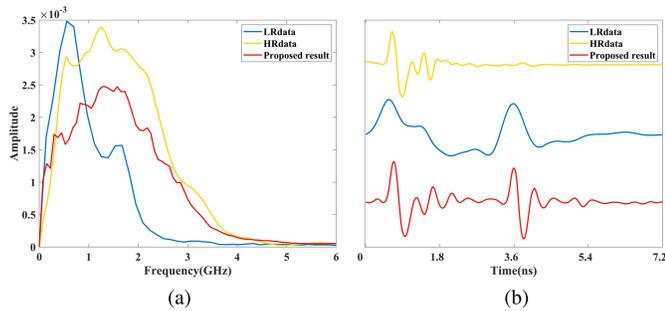
Fig. 17. Result analysis comparison for second lane data. (a) Multitrace average amplitude spectrum. (b) Time-domain waveforms for the 2800th single trace data.
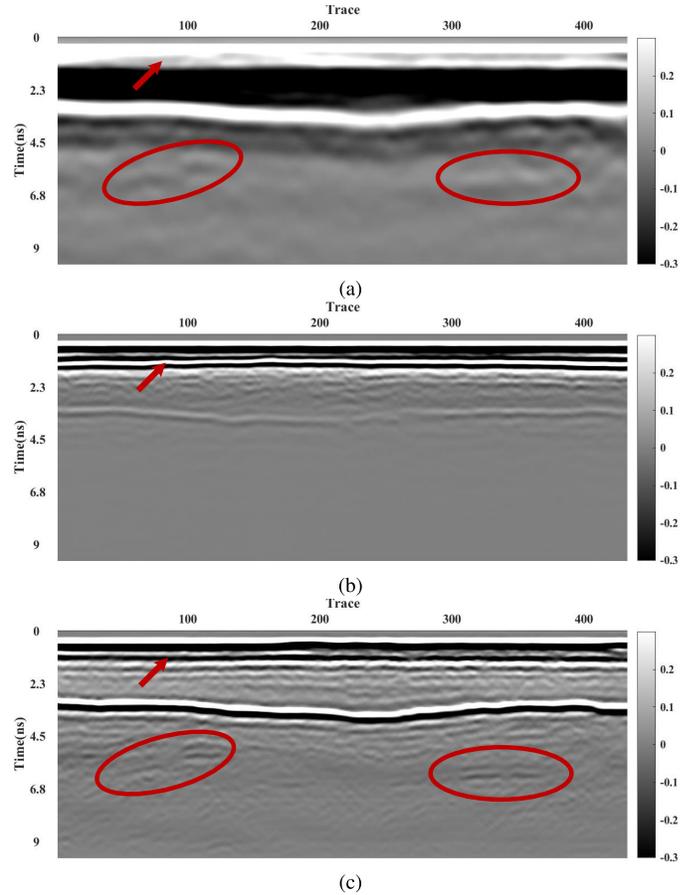

Fig. 18. Enlarged experimental results for second lane data from 2488th to 2900th traces. (a) Acquired low-resolution data. (b) Acquired high-resolution data. (c) Generated high-resolution data using weakly supervised learning.

low-resolution data but with an elevated resolution. This improvement is clearly demonstrated by more pronounced reflection wave signals in our experimental results, indicating that our method extracts finer information from deep layers and elevates deep-layer resolution to par with shallow-layer data from actual high-frequency radar exploration. This comparison underscores the effectiveness and superiority of our proposed method, especially under challenging conditions.

Fig. 17(a) presents the average amplitude spectrum comparison. The blue, yellow, and red lines represent the amplitude spectra of low-resolution, high-resolution, and our method-enhanced GPR data, respectively. By enhancing the resolution on actual low-resolution data, our method captures detailed subsurface features. It closely mirrors the amplitude spectrum of the high-resolution data with a broader frequency spectrum. Transitioning to Fig. 17(b), we examine the time-domain waveforms of individual 2800th traces from the three GPR datasets. The waveform generated by our method, symbolized by the red line, closely corresponds with the high-resolution data in the early time axis positions (1 ns), signifying enhanced resolution. In deeper subsurface regions, our method uncovers more valid information with pronounced fluctuations and finer details, similar to shallow low-resolution GPR data. This suggests our method can generate high-resolution GPR data with significant exploration depth, effectively balancing resolution and depth.

The low-resolution data mentioned above, ranging from the 2488th to the 2900th traces, are cropped and input into the network for testing and detailed comparison. The experimental results are shown in Fig. 18. Fig. 18(a) and (b) displays the collected actual low- and high-resolution GPR data, respectively. Comparing our results in Fig. 18(c) with them, it is evident that our method significantly enhances the GPR resolution and exhibits the following remarkable advantages. In the shallow subsurface positions indicated by the red arrow, our method effectively separates the blurred, thick stratum structures in the low-resolution data. Notably, the structures obtained around 1.5 ns closely resemble the subsurface layers of the actual high-resolution data and even exhibit distinguishably stronger energy, proving their reliability. At the position indicated by the red ellipses, our method captures fine features in the deep subsurface layers. This is demonstrated by accurately characterizing the medium reflection waves at that location.

3) Testing on Far Outside Lane Data: To evaluate the generalization performance of our network, we also test the

GPR data collected from the outermost lane (eighth lane). This is depicted in Fig. 19. A comparative analysis reveals that our proposed method considerably enhances the resolution, demonstrating reliable generalization ability. This enhancement is particularly notable in the middle and deep layers, where many valid subsurface information is recovered. This recovery suggests that our method can improve resolution and retrieve crucial subsurface details that might otherwise be lost or obscured in low-resolution data.

Collectively, these experiments underscore the effectiveness and reliability of our proposed method in enhancing GPR data resolution based on the transformation from low-resolution data, which provides valuable baseline information. Our proposed method offers the added advantages of faster processing speed and minimal human intervention. Notably, our method achieves this enhancement while facilitating a more profound exploration depth at a higher resolution. This dual achievement, resolution enhancement and deeper exploration, sets our method apart and illustrates its potential for significantly improving GPR data analysis and interpretation.

IV. DISCUSSION

Our method enhances resolution in GPR data through image-to-image translation, which has proven effective. However, several challenges remain to be addressed.
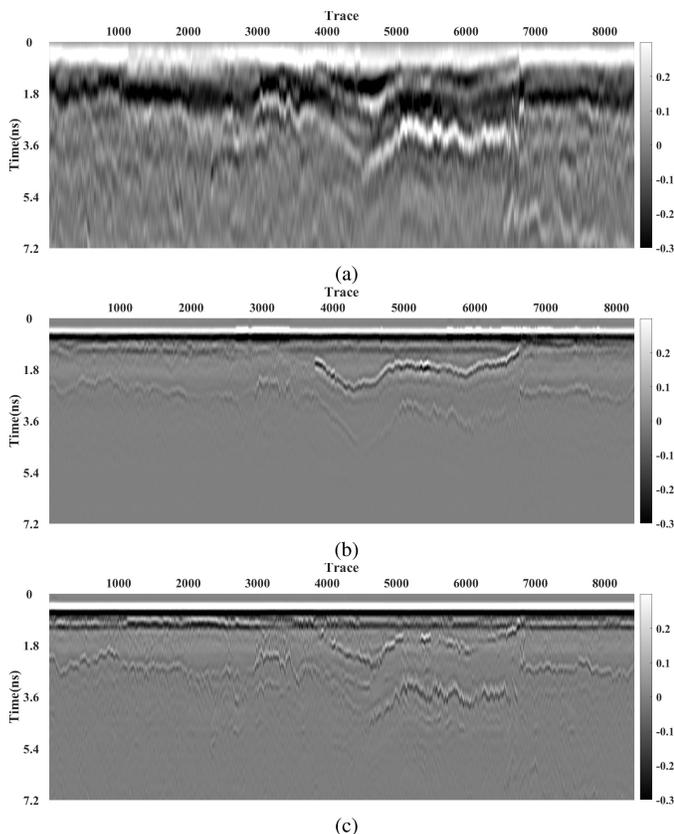
Fig. 19. Experimental results for data from far outside lane. (a) Acquired low-resolution data. (b) Acquired high-resolution data. (c) Generated high-resolution data using weakly supervised learning.

A. Preprocessing Limitations

A critical area of our methodology involves weakly supervised learning, which can sometimes be susceptible to inaccuracies due to the lack of precisely labeled training data. This can lead to the model developing biases or failing to generalize across different datasets. To counteract this, we plan to enrich our training data with more diverse examples.

Currently, our preprocessing techniques for GPR data include interpolation, normalization, and nonlinear data gain adjustments. However, we have not implemented techniques to address bad traces or suppress high-energy direct waves, which are crucial for enhancing data quality. The absence of a dedicated denoise module means our method may struggle with datasets heavily corrupted by coherent noise, often failing to recognize high-resolution features accurately and consequently producing artifacts post-enhancement. To address this, developing advanced noise suppression and trace correction techniques tailored for GPR data is necessary, which could significantly improve the clarity and usability of enhanced images.

B. Computational Efficiency

Our network model has a total parameter size of 339.2 MB, consisting of 113.2 MB of trainable parameters and 226.0 MB of non-trainable parameters. The total processing time on a single NVIDIA 3090 graphics processing unit for the simulated dataset and the first and second real-world datasets

is 41 348, 13 369, and 33 173 s, respectively. Undoubtedly, the substantial computational demand poses a significant limitation currently. Nevertheless, deep learning models demonstrate promising generalization capabilities for datasets with similar distributions. This offers the potential to process large-scale GPR datasets from similar geographical areas efficiently. To address the computational burden without compromising performance, we will explore more computationally efficient network architectures.

C. Lack of Physical Interpretation

Our current method lacks interpretability as it is purely data-driven. To improve this aspect, we plan to integrate traditional GPR processing methods with generative models. Embedding physical interpretations directly into the network architecture could offer a more intuitive and scientifically grounded approach to GPR data enhancement. In addition, simultaneous mapping of time domain and frequency domain data could provide more physical information for resolution enhancement to preserve geological continuity.

These steps will be pivotal in refining our method and extending its applicability and robustness in future research endeavors.

V. CONCLUSION

We present a novel GPR data resolution enhancement algorithm using weakly supervised learning. The algorithm aims to tackle a persistent challenge in GPR data acquisition: the trade-off between exploration depth and resolution. Our approach leverages the power of a CycleGAN network to learn the transformation from low-resolution GPR data into unpaired high-resolution data while preserving exploration depth. Successful simulated and real-world applications demonstrate the robustness and generalizability of our method. It offers practical advantages such as faster processing speed and minimal human intervention, making it a promising tool for real-world applications. Most importantly, our method offers an innovative, flexible acquisition strategy that eliminates the requirement for paired low- and high-resolution collections. This allows for collecting high-resolution data in proximity to low-resolution data along any path, significantly easing terrain and logistical constraints. Further research and refinement could focus on extending our method to more antennas with diverse frequencies and integrating the algorithm into mobile devices, paving the way for more accurate and efficient subsurface exploration.

REFERENCES

[1] M. Beres, A. Green, P. Huggenberger, and H. Horstmeyer, "Mapping the architecture of glaciofluvial sediments with 3-dimensional georadar," *Geology*, vol. 23, no. 12, pp. 1087–1090, 1995.

[2] M. Beres, P. Huggenberger, A. G. Green, and H. Horstmeyer, "Using two- and three-dimensional georadar methods to characterize glaciofluvial architecture," *Sedimentary Geol.*, vol. 129, nos. 1–2, pp. 1–24, Nov. 1999.

[3] W. Zhao et al., "Advances in GPR data acquisition and analysis for archaeology," *Geophys. J. Int.*, vol. 202, no. 1, pp. 62–71, Apr. 2015.

[4] L. B. Conyers and J. Leckebusch, "Geophysical archaeology research agendas for the future: Some ground-penetrating radar examples," *Archaeological Prospection*, vol. 17, no. 2, pp. 117–123, Apr. 2010.

[5] D. J. Daniels, "A review of GPR for landmine detection," *Sens. Imag., Int. J.*, vol. 7, no. 3, pp. 90–123, Sep. 2006.

[6] D. Hu, S. Li, J. Chen, and V. R. Kamat, "Detecting, locating, and characterizing voids in disaster rubble for search and rescue," *Adv. Eng. Informat.*, vol. 42, Oct. 2019, Art. no. 100974.

[7] R. Streich and J. van der Kruk, "Characterizing a GPR antenna system by near-field electric field measurements," *Geophysics*, vol. 72, no. 5, pp. A51–A55, Sep. 2007.

[8] C. Warren and A. Giannopoulos, "Creating finite-difference time-domain models of commercial ground-penetrating radar antennas using Taguchi's optimization method," *Geophysics*, vol. 76, no. 2, pp. G37–G47, Mar. 2011.

[9] B. Lampe and K. Holliger, "Effects of fractal fluctuations in topographic relief, permittivity and conductivity on ground-penetrating radar antenna radiation," *Geophysics*, vol. 68, no. 6, pp. 1934–1944, Nov. 2003.

[10] N. Economou and A. Vafidis, "Deterministic deconvolution for GPR data in the $t - f$ domain," *Near Surf. Geophysics*, vol. 9, no. 5, pp. 427–433, 2011.

[11] S. Gang, T. Yang-Jun, and Y. X. Hua, "Application study on the least square deconvolution in GPR signal processing," in *Proc. IEEE 2nd Int. Conf. Comput., Control Ind. Eng.*, vol. 2, Aug. 2011, pp. 398–401.

[12] C. Schmelzbach and E. Huber, "Efficient deconvolution of ground-penetrating radar data," *IEEE Trans. Geosci. Remote Sens.*, vol. 53, no. 9, pp. 5209–5217, Sep. 2015.

[13] T. Imai and T. Mizutani, "Reflectivity-consistent sparse blind deconvolution for denoising and calibration of multichannel GPR volume images," *IEEE Trans. Geosci. Remote Sens.*, vol. 61, pp. 1–10, 2023, Art. no. 5109610, doi: 10.1109/TGRS.2023.3317846.

[14] J. D. Irving and R. J. Knight, "Removal of wavelet dispersion from ground-penetrating radar data," *Geophysics*, vol. 68, no. 3, pp. 960–970, May 2003.

[15] L. Zhang, S. Liu, and J. Wu, "Layered media q estimation for GPR signal processing using the frequency shift method," in *Proc. Int. Conf. Comput. Appl. Syst. Model. (ICCASM)*, vol. 11, 2010, pp. V11–324.

[16] P. X. Neto and W. E. de Medeiros, "A practical approach to correct attenuation effects in GPR data," *J. Appl. Geophysics*, vol. 59, no. 2, pp. 140–151, Jun. 2006.

[17] F. A. Belina, B. Dafflon, J. Tronicke, and K. Holliger, "Enhancing the vertical resolution of surface georadar data," *J. Appl. Geophysics*, vol. 68, no. 1, pp. 26–35, May 2009.

[18] J. Tronicke, S. Schennen, and N. Allroggen, "Spectral enhancement of GPR data: Some practical considerations," in *Proc. 8th Int. Workshop Adv. Ground Penetrating Radar (IWAGPR)*, 2015, pp. 1–4.

[19] N. Economou and A. Vafidis, "Spectral balancing GPR data using time-variant bandwidth in the t-f domain," *Geophysics*, vol. 75, no. 3, pp. J19–J27, May 2010.

[20] J. H. Bradford, "Frequency-dependent attenuation analysis of ground-penetrating radar data," *Geophysics*, vol. 72, no. 3, pp. J7–J16, May 2007.

[21] J. H. Bradford and Y. Wu, "Instantaneous spectral analysis: Time-frequency mapping via wavelet matching with application to contaminated-site characterization by 3D GPR," *Lead. Edge*, vol. 26, no. 8, pp. 1018–1023, Aug. 2007.

[22] S. Sinha, P. Routh, and P. Anno, "Instantaneous spectral attributes using scales in continuous-wavelet transform," *Geophysics*, vol. 74, no. 2, pp. WA137–WA142, Mar. 2009.

[23] Y. Shi, B. Yu, H. Zhou, Y. Cao, W. Wang, and N. Wang, "FMG_INV, a fast multi-Gaussian inversion method integrating well-log and seismic data," *IEEE Trans. Geosci. Remote Sens.*, vol. 62, 2024.

[24] B. Yu, Y. Shi, H. Zhou, Y. Cao, N. Wang, and X. Ji, "Fast Bayesian linearized inversion with an efficient dimension reduction strategy," *IEEE Trans. Geosci. Remote Sens.*, vol. 62, pp. 1–10, 2024, Art. no. 4502910, doi: 10.1109/TGRS.2024.3360031.

[25] D. Liu, W. Wang, X. Wang, C. Wang, J. Pei, and W. Chen, "Poststack seismic data denoising based on 3-D convolutional neural network," *IEEE Trans. Geosci. Remote Sens.*, vol. 58, no. 3, pp. 1598–1629, Mar. 2020.

[26] D. Liu, Z. Deng, C. Wang, X. Wang, and W. Chen, "An unsupervised deep learning method for denoising prestack random noise," *IEEE Geosci. Remote Sens. Lett.*, vol. 19, pp. 1–5, 2022.

[27] O. M. Saad, Y. A. S. I. Oboué, M. Bai, L. Samy, L. Yang, and Y. Chen, "Self-attention deep image prior network for unsupervised 3-D seismic data enhancement," *IEEE Trans. Geosci. Remote Sens.*, vol. 60, pp. 1–14, 2022, Art. no. 5907014, doi: 10.1109/TGRS.2021.3108515.

[28] K. Wang, T. Hu, and B. Zhao, "An unsupervised deep neural network approach based on ensemble learning to suppress seismic surface-related multiples," *IEEE Trans. Geosci. Remote Sens.*, vol. 60, pp. 1–14, 2022, Art. no. 5924514, doi: 10.1109/TGRS.2022.3225809.

[29] S. Yu and J. Ma, "Deep learning for geophysics: Current and future trends," *Rev. Geophysics*, vol. 59, no. 3, Sep. 2021.

[30] D. Liu, M. D. Sacchi, X. Wang, and W. Chen, "Unsupervised deep learning for ground roll and scattered noise attenuation," *IEEE Trans. Geosci. Remote Sens.*, vol. 61, 2023, Art. no. 5920613.

[31] S. Liu, S. Cheng, and T. Alkhalifah, "Gabor-based learnable sparse representation for self-supervised denoising," 2023, *arXiv:2308.03077*.

[32] F. Qian et al., "Unsupervised seismic footprint removal with physical prior augmented deep autoencoder," *IEEE Trans. Geosci. Remote Sens.*, vol. 61, 2023.

[33] W. Zhan et al., "Simultaneous prediction of petrophysical properties and formation layered thickness from acoustic logging data using a modular cascading residual neural network (MCARNN) with physical constraints," *J. Appl. Geophysics*, vol. 224, May 2024, Art. no. 105362.

[34] K. Gao, C. Donahue, B. G. Henderson, and R. T. Modrak, "Deep-learning-guided high-resolution subsurface reflectivity imaging with application to ground-penetrating radar data," *Geophys. J. Int.*, vol. 233, no. 1, pp. 448–471, Aug. 2022.

[35] M.-S. Kang and Y.-K. An, "Frequency–wavenumber analysis of deep learning-based super resolution 3D GPR images," *Remote Sens.*, vol. 12, no. 18, p. 3056, Sep. 2020.

[36] C. Li and X. Li, "Attention mechanism based inversions for ground penetrating radar image," *Chin. J. Radio Sci.*, vol. 38, no. 5, pp. 825–834, 2023.

[37] S.-E. Hamran et al., "Radar imager for Mars' subsurface Experiment—RIMFAX," *Space Sci. Rev.*, vol. 216, no. 8, p. 128, Dec. 2020.

[38] C. Li et al., "Overview of the Chang'e-4 mission: Opening the frontier of scientific exploration of the lunar far side," *Space Sci. Rev.*, vol. 217, no. 2, p. 35, Mar. 2021.

[39] A. D. Booth, A. L. Endres, and T. Murray, "Spectral bandwidth enhancement of GPR profiling data using multiple-frequency compositing," *J. Appl. Geophysics*, vol. 67, no. 1, pp. 88–97, Jan. 2009.

[40] G. Lu, W. Zhao, E. Forte, G. Tian, Y. Li, and M. Pipan, "Multi-frequency and multi-attribute GPR data fusion based on 2-D wavelet transform," *Measurement*, vol. 166, Dec. 2020, Art. no. 108243.

[41] W. Zhao, L. Yuan, E. Forte, G. Lu, G. Tian, and M. Pipan, "Multi-frequency GPR data fusion with genetic algorithms for archaeological prospection," *Remote Sens.*, vol. 13, no. 14, p. 2804, Jul. 2021.

[42] F. Soldovieri and L. Orlando, "Novel tomographic based approach and processing strategies for GPR measurements using multifrequency antennas," *J. Cultural Heritage*, vol. 10, pp. e83–e92, Dec. 2009.

[43] G. Roncoroni, E. Forte, and M. Pipan, "Merging gated frequency-modulated continuous-wave Mars2020 RIMFAX ground-penetrating radar data," *Geophysics*, vol. 88, no. 2, pp. A7–A12, Mar. 2023.

[44] G. Roncoroni, E. Forte, I. Santin, and M. Pipan, "Deep learning-based multifrequency ground penetrating radar data merging," *Geophysics*, vol. 89, no. 1, pp. F1–F9, Jan. 2024.

[45] Y. Yuan, S. Liu, J. Zhang, Y. Zhang, C. Dong, and L. Lin, "Unsupervised image super-resolution using cycle-in-cycle generative adversarial networks," in *Proc. IEEE/CVF Conf. Comput. Vis. Pattern Recognit. Workshops (CVPRW)*. Salt Lake City, UT, USA: IEEE, 2018, pp. 814–81409.

[46] D. Liu, W. Niu, X. Wang, M. D. Sacchi, W. Chen, and C. Wang, "Improving vertical resolution of vintage seismic data by a weakly supervised method based on cycle generative adversarial network," *Geophysics*, vol. 88, no. 6, pp. V445–V458, Nov. 2023.

[47] J.-Y. Zhu, T. Park, P. Isola, and A. A. Efros, "Unpaired image-to-image translation using cycle-consistent adversarial networks," in *Proc. IEEE Int. Conf. Comput. Vis.*, Oct. 2017, pp. 2223–2232.

[48] Y. Zhang, S. Liu, C. Dong, X. Zhang, and Y. Yuan, "Multiple cycle-in-cycle generative adversarial networks for unsupervised image super-resolution," *IEEE Trans. Image Process.*, vol. 29, pp. 1101–1112, 2020.

[49] D. Ulyanov, A. Vedaldi, and V. Lempitsky, "Instance normalization: The missing ingredient for fast stylization," 2017, *arXiv:1607.08022*.

[50] S. Ioffe and C. Szegedy, "Batch normalization: Accelerating deep network training by reducing internal covariate shift," in *Proc. 32nd Int. Conf. Mach. Learn.*, F. Bach and D. Blei, Eds., vol. 37. Lille, France: PMLR, Jul. 2015, pp. 448–456.

[51] U. Demir and G. Unal, "Patch-based image inpainting with generative adversarial networks," 2018, *arXiv:1803.07422*.

[52] X. Mao, Q. Li, H. Xie, R. Y. Lau, and Z. Wang, "Multi-class generative adversarial networks with the L2 loss function," 2016, *arXiv:1611.04076*.

[53] I. Goodfellow et al., "Generative adversarial nets," in *Proc. Adv. Neural Inf. Process. Syst.*, vol. 27, 2014, pp. 1–12.

[54] Z. Wang, E. P. Simoncelli, and A. C. Bovik, "Multiscale structural similarity for image quality assessment," in *Proc. 37th Asilomar Conf. Signals, Syst. Comput.*, Pacific Grove, CA, USA, vol. 2, Nov. 2003, pp. 1398–1402.

[55] D. P. Kingma and J. Ba, "Adam: A method for stochastic optimization," 2014, *arXiv:1412.6980*.

[56] C. Warren, A. Giannopoulos, and I. Giannakis, "GprMax: Open source software to simulate electromagnetic wave propagation for ground penetrating radar," *Comput. Phys. Commun.*, vol. 209, pp. 163–170, Dec. 2016.

[57] J. W. J. Hosken, "Ricker wavelets in their various guises," *1st Break*, vol. 6, no. 1, Jan. 1988.

[58] L. Xiang, H.-L. Zhou, Z. Shu, S.-H. Tan, G.-Q. Liang, and J. Zhu, "GPR evaluation of the damaoshan highway tunnel: A case study," *NDT E Int.*, vol. 59, pp. 68–76, Oct. 2013.

Zhensheng Shi received the M.S. degree in electromagnetic fields and microwave technology from Xi'an Jiaotong University (XJTU), Xi'an, China, in 1989.

He is currently a Senior Engineer with the School of Electronic and Information Engineering, XJTU. His research interests include RF, microwave circuit design, and radar signal processing and imaging.

Dawei Liu received the bachelor's degree in communication engineering from Chang'an University, Xi'an, China, in 2013, the master's degree in electronic and communication engineering from Xi'an Jiaotong University (XJTU), Xi'an, in 2018, and the Ph.D. degree from the School of Information and Communication Engineering from Xi'an Jiaotong University, in September 2022.

From 2022 to 2023, he was a Post-Doctoral Scholar with the Department of Earth, Atmospheric, and Planetary Sciences, Purdue University, West Lafayette, IN, USA. He is currently a Post-Doctoral Fellow with the Department of Physics, University of Alberta, Edmonton, AB, Canada. His research interests include tensor decomposition, deep learning, and time-frequency analysis and their applications in the seismic data processing.

Dr. Liu is a reviewer for IEEE TRANSACTIONS ON GEOSCIENCE AND REMOTE SENSING, *Geophysics*, *Acta Geophysica*, and *Petroleum Science*.

Mei Zhou, photograph and biography not available at the time of publication.

Xiaokai Wang (Member, IEEE) received the bachelor's degree in information engineering and the Ph.D. degree in communication engineering from Xi'an Jiaotong University (XJTU), Xi'an, China, in 2006 and 2012, respectively.

From 2012 to 2014, he was a Post-Doctoral Fellow with the Institute of Geology and Geophysics, Chinese Academy of Sciences, Beijing, China. He joined the Department of Computational Geophysics, XJTU, in 2015, where he was transferred to the School of Information and Communication Engineering, in 2018. He was a Visitor of the Bureau of Economic Geology, The University of Texas at Austin, Austin, TX, USA, from 2016 to 2017. His research interests include seismic attributes extraction, and time-frequency analysis and their applications in seismic data processing.

Mauricio D. Sacchi (Member, IEEE) received the Diploma degree in geophysics from the National University of La Plata, La Plata, Argentina, in 1988, and the Ph.D. degree in geophysics from The University of British Columbia (UBC), Vancouver, BC, Canada, in 1996.

He joined the Department of Physics, University of Alberta, Edmonton, AB, Canada, in 1997. He directs the Signal Analysis and Imaging Group, Edmonton, an initiative for advanced research for geophysical signal processing and imaging. He has developed and taught short courses for industry and professional associations. His research interests include geophysical signal analysis and seismic imaging methods.

Dr. Sacchi was a recipient of the 2012 Medal of the Canadian Society of Exploration Geophysicists (CSEG), the 2014 Central and South America Honorary Lecturer for the Society of Exploration Geophysicists, the 2016 CSEG Distinguished Lecturer, and the 2019 Virgil Kauffman Gold Medal. He was the Editor-in-Chief of the journal *Geophysics* from 2016 to 2018.

Wenchao Chen received the B.S. and M.S. degrees in seismic exploration and information technology from Chang'an University, Xi'an, China, in 1993 and 1996, respectively, and the Ph.D. degree in electromagnetic field and microwave technology from Xi'an Jiaotong University, Xi'an, in 2000.

From 2000 to 2002, he was a Post-Doctoral Fellow with the Department of Computation Science, Northwestern Polytechnical University, Xi'an. Since 2002, he has been with the School of Information and Communications Engineering, Xi'an Jiaotong University, where he is currently a Professor. His research interests include seismic and ground-penetrating radar (GPR) signal processing, blind signal processing, and sparse representation.

Dr. Chen has served as a member of the Society of Exploration Geophysicists (SEG) and Chinese Geophysical Society. He is also a referee for several journals, including the IEEE JOURNAL OF SELECTED TOPICS IN APPLIED EARTH OBSERVATIONS AND REMOTE SENSING, IEEE TRANSACTIONS ON GEOSCIENCE AND REMOTE SENSING, *Geophysics*, *Interpretations*, and *Journal of Applied Geophysics*.

Zhaodan Liu, photograph and biography not available at the time of publication.

Xian Wang, photograph and biography not available at the time of publication.